ACS APPLIED ELECTRONIC MATERIALS

pubs.acs.org/acsaelm Article

Correlation between Material Properties, Crystalline Transitions, and Point Defects in RF Sputtered (N,Mg)-Doped Copper Oxide Thin Films

Thomas Ratz,* Emile Fourneau, Naama Sliti, Cedric Malherbe, Amaury Baret, Benedicte Vertruyen, Alejandro V. Silhanek, and Ngoc Duy Nguyen

Cite This: https://doi.org/10.1021/acsaelm.4c01396 Read Online

ACCESS | Metrics & More | Article Recommendations | Supporting Information

ABSTRACT: In the present work, we investigate the effects of N and Mg doping on the optical and electrical properties of Cu_2O thin films deposited using radiofrequency magnetron sputtering at room temperature. Additionally, crystalline phases are studied through complementary X-ray diffraction and energy dispersive X-ray spectroscopy measurements. It is shown that nitrogen incorporation enhances both the electrical and optical properties, with resistivity reaching a value as low as 1.15 Ωcm and an average transmittance in the visible range of 31.74%. Raman spectroscopy measurements indicate an increase in the number of $(N_2)_{Cu}$ shallow acceptor point defects, explaining the probed enhancement of p-type majority charge carriers. Also, in Mg-doped samples, marginal improvement of the optoelectrical properties is established. Conversely, we demonstrate that co-doping with Mg and N degrades the material crystallinity, leading to a reduction of thin film conductivity that could be attributed to high nitrogen incorporation. Subsequently, the influence of dopants on the electrical and optical properties is discussed via the analysis of the correlation between defects and Raman activities in the studied copper oxide thin films. This work contributes to the assessment of Mg and N as doping species, unveiling the dominant behavior of specific point defects. The results obtained in the study can therefore benefit future developments in copper-based p-type semiconducting oxides with enhanced optical and electrical properties.

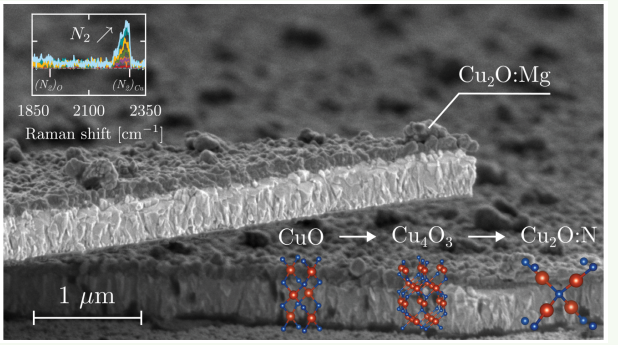

KEYWORDS: *copper oxide, nitrogen doping, magnesium doping, co-doping, RF sputtering, Raman, defects, phases, transparent conducting oxides (TCO)*

INTRODUCTION

Cu_2O copper oxide belongs to a broad class of semiconductors termed transparent conducting oxides (TCOs). The vast majority of them are n-type crystals exhibiting commercial grade electrical and optical performances.[1] However, their p-type counterparts, essential for transparent electronics, face important challenges hampering the development of efficient optoelectrical devices.[2] These limitations are partially caused by the low charge carrier mobility, lying between 1 and 100 $cm^2\ V^{-1}\ s^{-1}$, as a consequence of the localized nature of the 2p oxygen orbital in most oxides.[2,3] Cu_2O is also a promising candidate for photovoltaic (PV) applications, as this material exhibits a large absorption coefficient on the order of $10^4\ cm^{-1}$ and p-type conductivity with charge carrier concentration on the order of 10^{14} to $10^{17}\ cm^{-3}$. Additionally, this material is abundant and nontoxic and can be synthesized using various chemical and physical routes.[4,5] Cu_2O is therefore well suited for PV application with a Shockley−Queisser (SQ) efficiency limit of 20.5%, considering a 2.1 eV band gap as experimentally measured by Jolk et al. via excitonic absorption.[6−8] Over the past 20 years, the efficiency of copper oxide based solar cells notably increased from 2% to the current world record of 8.4%, reported by Shibasaki et al. in 2021.[8−10] However, there remains a significant margin for improvement concerning the PV performance of this earth-abundant material.[10] Despite recent improvements, the efficiency is still limited by the open-circuit voltage (V_{OC}) and the fill factor (FF) values.[9−17] The former results from charge recombination processes in the bulk and at the interfaces, while the latter is partially associated with the poor electrical performances of the copper oxide absorber layer.[4,5,18] In order to circumvent these limitations, a deeper

Received: August 8, 2024
Revised: December 5, 2024
Accepted: December 5, 2024

Table 1. Recent Assessment of Point Defects in Copper Oxide Films[a]

Defect type	Defect	ΔH_F [eV]	Behavior	E_T [eV]	Raman activity [cm^{-1}]	Expt	Theo
Vacancy	V_{Cu}	Low	Acceptor, delocalized hole	0.23	↓ 515 (T_{2g}) ↑ 541, (318, 510) (A_{1g}, E_g)	25	21, 26, 27
	$V_{Cu,split}$	Low	Deep acceptor, localized hole	0.47	All	25	21, 27
	V_O	/	Possible hole killer	/	All except 90 (T_{2u})	28	26, 29
Substitution	Cu_O	/	/	/	All except 90 (T_{2u})	/	26
	O_{Cu}	/	/	/	↓ 515 (T_{2g}) ↑ 541, (318, 510) (A_{1g}, E_g)	/	26
Interstitial	$I_{O,oct}$	High	Deep	1.08	↓ 515 (T_{2g}) ↑ 541, (318, 510) (A_{1g}, E_g)	25	27
	$I_{O,tetr}$	High	Deep	1.27	All	25	27
	I_{Cu}	/	/	/	/	/	/
Extrinsic	Mg on $V_{Cu,split}$	Spontaneous (<0)	Indirect acceptor, V_{Cu}	/	/	20	19
	$(N_2)_{Cu}$	Low	Acceptor	0.2	2280		24
	$(N_2)_O$	High	Deep donor	0.38	1309, 1929		24
	N_O	Low	Deep acceptor	0.53	/		24, 30

[a]The defect type and the chemical species involved are highlighted, as well as the corresponding formation energy. Since this quantity is a function of the material stoichiometry, a qualitative value labelled *low* (below 1.5 eV) or *high* (above 1.5 eV) is provided. The behavior or character of a given defect is qualified as either acceptor, donor, or deep. The latter qualification underlines the possible behavior of the defect as a recombination center. The Raman bands of the reported defects are also provided with the corresponding phonon modes (90, 110, 145, 155, 320, 515, 620, 655 cm^{-1} as described in refs 26 and 31). The two last columns show the corresponding experimental or theoretical works reported in the literature.

understanding of the microscopic mechanisms ruling the material's conductivity and its link to point defects is needed. In addition, as widely reported in recent years, material doping offers an interesting strategy first to inhibit the presence of defects acting as recombination centers and, second, to boost the material optoelectrical properties. Among possible doping species, as presented in the following, Mg and N appear as suitable elements in the case of copper oxide.[19−24]

As reported in Table 1, Cu_2O presents a variety of intrinsic point defects: vacancies (V_{Cu}, $V_{Cu,split}$, and V_O), substitutions (O_{Cu} and Cu_O), and interstitials (I_{Cu}, I_O, and $I_{O,oct}$) with different impacts on the material properties.[25,27,29,32] In 2006, Nolan et al. identified two kinds of Cu vacancies, respectively V_{Cu}, which leaves two oxygen atoms with three bonds instead of four, and $V_{Cu,split}$, resulting from the displacement of a neighbor copper atom toward the copper vacancy site, allowing the four-bonds state to be recovered.[19] Using first-principles calculations, they studied the p-type conductivity in copper oxide, reporting V_{Cu} as the origin of the delocalized hole states participating in the material conductivity.[21,27] Later on, in 2009, Scalon et al. underlined that both copper vacancies behave as shallow defects participating in the material p-type conductivity with formation energies below 1.5 eV. Using deep level transient spectroscopy (DLTS), Paul et al. reported on transition energy levels at 0.22 and 0.45 eV above the valence band for respectively V_{Cu} and $V_{Cu,split}$.[25] In contrast, both oxygen interstitials (I_O and $I_{O,oct}$) are associated with defect energy levels located at about the center of the material band gap but exhibiting high formation energies in the range from 1.5 to 2 eV. Concerning the copper interstitial, a high formation energy was reported by Raebiger et al. More specifically, they reported the anionic oxygen vacancy V_O as a potential *hole killer*. However, its efficiency in this role is debated: Raebiger et al. present V_O as inefficient due to its lack of transition level inside the material band gap,[29] whereas Sekkat et al. point out V_O as responsible for the decreasing hole concentration reported in refs 28 and 33.

Concerning Mg incorporation in copper oxide, Isseroff et al. used hybrid DFT to study the doping of Cu_2O.[19] These authors demonstrated that the simple copper vacancy V_{Cu} produces a delocalized hole, while the split vacancy $V_{Cu,split}$ generates a localized hole. This localized hole plays a key role in the origin of the minority carrier trapping in copper oxide. The split vacancy could therefore inhibit the diffusion of minority carriers, acting as a trap state. The authors of ref 19 suggested that these specific trap states can be prevented by doping the material with Li, Mg, Mn, or Zn, resulting in single vacancies and promoting delocalized holes. These predictions have been further confirmed by experimental work using both physical and chemical routes for the synthesis of the Cu_2O layers.[20,34−36]

Moreover, in 2015, using hybrid density functional theory, Thienprasert et al. studied the nitrogen-related defects in copper oxide. Among them, substitutions N_O and $(N_2)_{Cu}$ were identified as the most dominant ones with formation energies lower than 1.5 eV.[24] Moreover, N_O and $(N_2)_{Cu}$ are identified as acceptor-type defects with transition energy levels, respectively, of 0.53 and 0.2 eV above the valence band. Zhao et al. also discussed that the substitution of oxygen by nitrogen N_O could create a new absorption peak near 0.9 eV.[30] In addition to a range of predictive studies, several works also successfully achieved N-doped Cu_2O thin films using various synthesis techniques.[22,23,37−39] Using postoxidation processes in oxygen−nitrogen plasma, Li et al. reported a high concentration of nitrogen interstitials (I_N) as well as N_O and V_O. However, in their work, Thienprasert et al. reported formation energies higher than 1.5 eV for each nitrogen interstitial type.[24] Moreover, in 2023, Mudhaffar et al. reported through photoluminescence (PL) measurement, a lower V_O content and fewer Cu dangling bonds produced by ion bombardment via the sputtering. They interpreted those results as the filling of oxygen vacancies with nitrogen N_O.

Building on the reported improvements in the material properties from individual nitrogen and magnesium doping, the objective of this work is to extend the scientific community's understanding of the role of point defects in singly doped copper oxide materials. Additionally, we aim to further enhance the material optoelectrical performance through (N,Mg) co-doping. We investigate the (N,Mg) co-doping of copper oxide thin films deposited using RF magnetron sputtering at room temperature. To the best of our knowledge, there is no previous work reporting on this specific co-doping in Cu_2O layers, and it is worth noticing that this co-doping was successfully implemented in another Cu-

https://doi.org/10.1021/acsaelm.4c01396
ACS Appl. Electron. Mater. XXXX, XXX, XXX−XXX

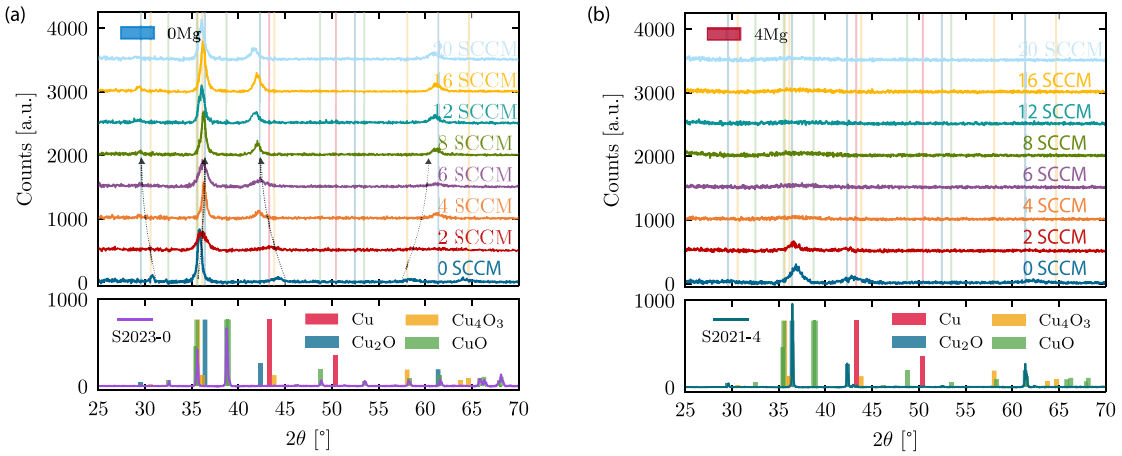

Figure 1. Crystallographic characterization of (a) N-doped (S2023-0, blue highlight) and (b) (N,Mg)-doped (S2021-4, red highlight) thin films deposited using a N_2 flow varying between 0 and 20 sccm. The top panels show the XRD measurements of the films, and the bottom panel provides the XRD characterization of the sputtering targets themselves as well as the main copper oxide phases also reported in the top panel to facilitate the phase identification. In (a), the arrows present a guide to the eye concerning the observed crystalline transition from Cu_4O_3 to Cu_2O.

based material: $CuCrO_2$ as reported in ref 40. In the following, we first present the methodology used to synthesize and characterize the copper oxide layers. Then, we report and discuss the optoelectrical results obtained for the N,Mg doping processed thin films whose crystalline structures were previously characterized. Then, in a subsequent development, we correlate the optoelectrical properties, the crystalline structure, and the material point defects through the wide range of characterization techniques.

SAMPLE SYNTHESIS AND CHARACTERIZATION

Copper oxide thin films were deposited by RF magnetron sputtering in sputter up configuration at room temperature (RT). The deposition was performed on 1.5 × 1.5 cm^2 glass substrates previously cleaned in an ultrasonic bath using acetone followed by isopropyl alcohol (IPA) treatment (5 min each). Prior to deposition, a presputtering step corresponding to a 30 nm thickness was performed under a nominal base pressure on the order of 1 × 10^{-4} mTorr. The specific deposition parameters of each sample are listed in Table S1 of the Supporting Information (SI). The Mg content was tuned using two different 2 in. ceramic sputtering targets (99.99% purity): undoped (CuO, S2023-0) and doped (Cu_2O, S2021-4, ∼4 w/w%: Mg), with the Mg content expressed via the Cu/[Cu + Mg] mass ratio (see Figure S1 in SI). During the deposition, a plasma pressure of 5 mTorr, a constant flow of 20 sccm of Ar, and a variable flow of N_2 between 0 and 20 sccm were used along with a sputtering power of 69 W without substrate rotation. As a result, the synthesized samples are close to 200 nm in thickness. The investigation presented in this work relies on a preliminary optimization of the RF magnetron sputtering plasma pressure presented in the SI (see Figure S2). In addition, a thorough crystallographic characterization of the targets is also presented (see SI).

Subsequently to the fabrication of the samples, two main types of characterizations were performed. First, the optical properties were measured using a UV−vis 3600 Shimadzu spectrophotometer equipped with an integrating sphere, while a PhysTech RH 2035 Hall measurement system was used for electrical measurements. Transmittance measurements were performed for wavelengths between 200 and 1600 nm by ensuring a proper baseline realized in air. The arithmetic mean transmittance value was computed in the visible wavelength range between 380 and 750 nm as the mean transparency value. Electrical measurements were performed on samples under the Van der Pauw configuration at room temperature using a static magnetic field of 0.4 T for the Hall measurement. Then, the samples were analyzed by X-ray diffraction (XRD), Raman, and energy dispersive X-ray (EDX) spectroscopies. In a second step, crystallographic characterizations were carried out with a Bruker Twin−Twin diffractometer in grazing incidence configuration (incident angle 1°) for 2θ angles between 25° and 70° with a Cu Kα source. Concerning the Raman characterization, the focus was set on the Raman shifts between 90 and 2600 cm^{-1} using a 532 nm laser source and a power of 0.4 mW. Finally, the EDX measurements were performed on a Tescan Vega 3 scanning electron microscope SEM-EDS system. Further details concerning the characterizations performed on the samples are provided in the SI.

RESULTS AND DISCUSSION

Crystallographic Characterization. We initiate the presentation of the results with the XRD characterization of the undoped (0Mg) and Mg-doped (4Mg) samples as nitrogen is introduced with a N_2 flow between 0 and 20 sccm. First, as depicted in Figure 1(a), concerning the S2023-0 synthesized layers (0Mg), at 0 sccm, we report a Cu_4O_3 crystallinity followed by a crystalline shift to Cu_2O as the nitrogen flow is increased from 0 to 4 sccm. The dominant peak located around 36° is shifted to higher values, while XRD peaks located just above 30° and below 45° are respectively translated toward 29° and 43° as illustrated by the arrows. Consequently, starting from the target CuO crystal phase (see SI), the desired sample crystallinity (Cu_2O) is achieved for nitrogen flow values higher than 4 sccm. From this observation, we emphasize both the change of crystallinity that occurs first, (i) from the target to the 0 sccm layer (following the sputtering deposition) and, second, (ii) upon nitrogen doping. In a later section, the crystalline phase transition discussed will be further validated through Raman characterizations. The reduction of the oxygen content inside the grown layer (Cu_4O_3) with respect to the S2023-0 sputtering target (CuO) could be attributed to the lack of oxygen flow during the material deposition.[10,33,41,42] Fur-

https://doi.org/10.1021/acsaelm.4c01396
ACS Appl. Electron. Mater. XXXX, XXX, XXX−XXX

thermore, in 2020, Patwary et al. reported on the nitrogen doping of Cu_4O_3 thin films without observing any material phase transition.[43] However, in their work, the authors described an additional oxygen regulation during reactive sputtering deposition. As a result, the control of this parameter could explain the absence of the crystallinity change. Moreover, as this second crystalline transition is observed for an increased nitrogen flow between 0 and 4 sccm, this could also reveal a possible interaction between nitrogen and oxygen through the formation of N_O point defects.[22] In the Supporting Information, we present, for the N-doped thin films, crystallite sizes ranging from 8 to 15 nm (Table S4).

In contrast, as presented in Figure 1(b) for the Mg-doped samples prepared by using a Mg-doped Cu_2O target, a Cu_2O material phase was obtained for each nitrogen flow. Based on a first comparison between the 0 sccm thin films presented in Figure 1(a) and (b), we observe a lower material crystallinity in the case of the Mg doping. Then, a rapid degradation of the film crystallinity as the nitrogen flow increased was observed upon both Mg and N doping, as shown in Figure 1(b). Indeed, for nitrogen flow above 2 sccm, the samples' behavior tends toward amorphous-like layers with a peak around 36° spreading over a broad 2θ range.

Elemental Composition. In Figure 2, we present the evolution of the sample stoichiometries as estimated from EDX

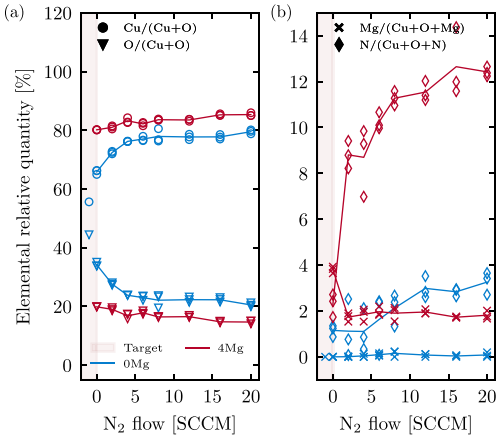

Figure 2. Relative elemental composition of N-doped (S2023-0, blue highlight) and (N,Mg)-doped (S2021-4, red highlight) thin films deposited using a N_2 flow varying between 0 and 20 sccm. We present (a) the Cu and O relative compositions as well as (b) the N and Mg relative compositions for both the sputtering targets (first point, transparent red highlight) and the deposited samples. The overall accuracy concerning the relative stoichiometries obtained is on the order of ±2%.[44] Elemental compositions are correlated to the results obtained from XRD, EDX, and TOF-SIMS measurements (see SI).

analysis, starting from the sputtering target (red background highlight), proceeding to the nitrogen undoped thin films, and finally reaching N-doped layers as the N is incorporated via the N_2 flow increase to 20 sccm. In Figure 2(a), the Cu and O relative stoichiometries are presented, whereas Figure 2(b) displays the relative compositions of the nitrogen and magnesium doping species. It is relevant to note that quantification of low atomic number elements such as nitrogen or oxygen by EDX reveals trends rather than accurate values. Moreover, unlike bulk sputtering target measurements, the characterization of 200 nm-thick films includes contributions from the glass substrate. Nevertheless, the measurements presented in this work are well supported by time-of-flight secondary ion mass spectrometry (TOF-SIMS) measurements realized on the same layers and presented in the SI. Therefore, in the following, we discuss the trends in the sample's elemental compositions by correlating the results obtained from XRD, EDX and TOF-SIMS measurements.

In Figure 2(a), upon nitrogen doping of the Mg-free Cu_2O samples (blue curve, 0Mg), we observe an increase of the Cu content and a decrease of the O content before reaching a plateau for N_2 flows above 4 sccm. The reported trend is in good agreement with the crystalline phase transitions determined from the XRD results: first (i) from CuO to Cu_4O_3 (from the sputtering target to the 0 N_2 flow thin film) and, second, (ii) from Cu_4O_3 to Cu_2O. Concerning the nitrogen incorporation, as shown in Figure 2(b) (blue curve, 0Mg), we report first a negligible amount inside the synthesized layer for N_2 flow values between 0 and 4 sccm. In contrast, for values above 4 sccm, an increased nitrogen inclusion is observed followed by a plateau for N_2 values above 12 sccm.

Regarding the Mg-doped thin films, following the nitrogen flow increase, a slight decrease (respectively increase) of the O content (respectively Cu content) is observed. However, as reported in the XRD measurements, the Cu_2O crystalline phase seems to be conserved. Concerning the doping species, in Figure 2(b), it is possible to observe a Mg reduction from 4% to 2% upon nitrogen incorporation. Corroborating this observation, Resende et al. also reported a reduction of the Mg content inside the synthesized thin film with a value 2.3 times lower with respect to the Mg content in the prepared solution.[20] Moreover, each sample deposited with a nonzero N_2 flow presents an equivalent Mg stoichiometry. As previously underlined based on the XRD observations, we further suspect, based on the Mg stoichiometry reduction upon nitrogen incorporation, a possible interaction between the N and Mg doping species. Finally, concerning the nitrogen content in the films, we report a drastic increase of the elemental composition first from 0 to 2 sccm (reaching a value of 9%). This observation is put into perspective with the 1% nitrogen incorporation reported for the Mg undoped sample for the same N_2 flow. As the N_2 flow increases, constant nitrogen incorporation is observed until a maximum value of ∼12%. The magnitude of this incorporation is nearly four times larger in the Mg-doped layers in contrast to the 0Mg synthesized samples. In addition, the trends extracted from the EDX analysis are corroborated by the TOF-SIMS characterizations presented in the SI. These results suggest that such a large nitrogen incorporation could be facilitated by the presence of Mg and responsible for the amorphization of the (N,Mg)-doped samples. Below, we present a possible explanation for such observation by harnessing the knowledge acquired from each characterization technique.

Electrical and Optical Properties. From the knowledge acquired concerning the material crystal structure and elemental composition, we now present and discuss the results obtained for the electrical characterizations. In Figure 3(a) and (b), the p-type charge carrier concentrations and mobilities are displayed to support the thin film resistivity variations presented in Figure 3(c). Concerning the (Mg,N)-free sample, a p-type resistivity of 192 Ωcm corresponding to a mobility and charge carrier concentration of respectively 7.71×10^{16} cm^{-3} and 0.48 $cm^2\ V^{-1}\ s^{-1}$ is reported. The electrical behavior reported here is in good agreement with state-of-the-art copper

https://doi.org/10.1021/acsaelm.4c01396
ACS Appl. Electron. Mater. XXXX, XXX, XXX−XXX

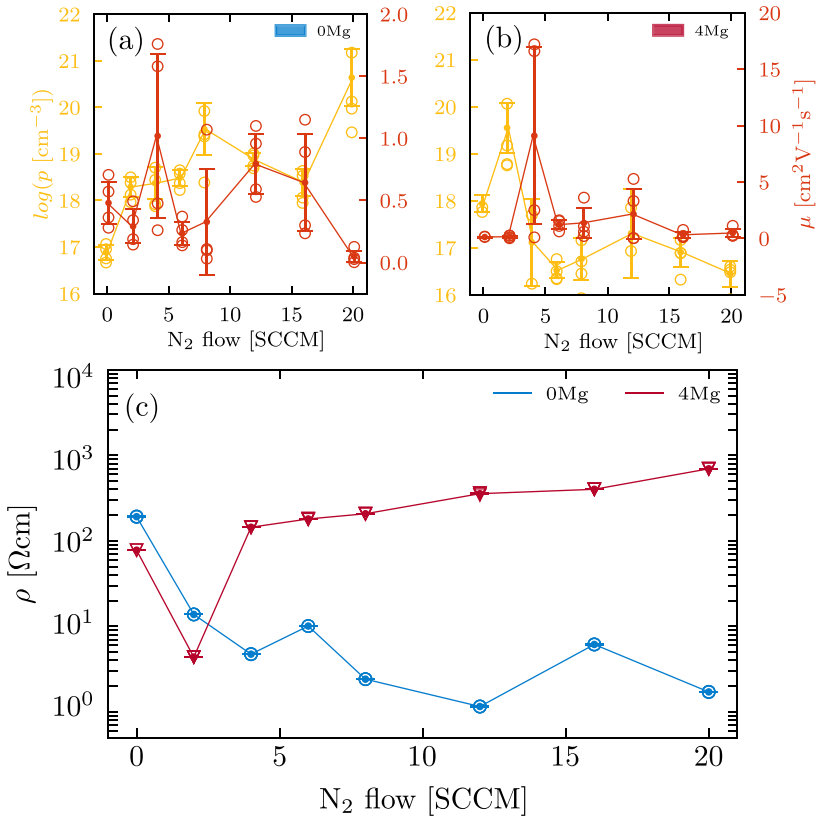

Figure 3. Electrical characterization of N-doped (S2023-0, blue-highlighted "0Mg" data) and (N,Mg)-doped (S2021-4, red-highlighted "4Mg" data) thin films deposited using a N_2 flow varying between 0 and 20 sccm. In (a) and (b) the thin film majority charge carrier concentration and mobility corresponding to the N-doped and (N,Mg)-doped thin films are presented as a function of the N_2 flow. In panel (c), the resulting thin film resistivity is provided for each study (maximum relative error is 2.1%).

oxide resistivity values on the order of 100 Ωcm obtained in several works.[20,23,35,38]

As shown in Figure 3(c), without Mg and upon incorporation of N via an increasing flow from 0 to 4 sccm, we identify a 2 orders of magnitude decrease in resistivity with a resulting value as low as 4.7 Ωcm. From Figure 3(a), we attribute this decrease mainly to the nearly 2 orders of magnitude increase in charge carrier concentration from 7.7×10^{16} cm^{-3} to 2.3×10^{18} cm^{-3}. As the nitrogen flow is further increased above 4 sccm, a slight reduction of the material resistivity to 1.15 Ωcm is identified for a N_2 flow of 12 sccm. The resistivity behavior for nitrogen flows above 4 sccm is attributed to a constant increase of the charge carrier concentration to a maximal value of 4.4×10^{20} (20 sccm) and to a decrease of the mobility to ~0.1 cm^2 V^{-1} s^{-1} (see Figure 3(a)). Overall, the nitrogen incorporation for low N_2 flow leads first to a large decrease of the material resistivity followed by a slight improvement, ending up in a saturation value between 1 and 10 Ωcm. These observations are corroborated by similar electrical improvements reported in the literature as nitrogen is introduced in Cu_2O samples synthesized using various growth processes.[22,23,37,38]

Focusing our attention on the two 0 sccm data points corresponding to the evolution of the resistivity upon Mg doping, we report a decrease of resistivity from 191.7 Ωcm to 77.8 Ωcm. Comparing Figure 3(a) and (b), this evolution is caused by a dominant charge carrier concentration increase from 7.7×10^{16} to 8.7×10^{17} cm^{-3} and slightly counterbalanced by a mobility decrease from 0.5 to 0.1 cm^2 V^{-1} s^{-1}. In a previous study, we also reported that the Mg incorporation leads to a nearly two-orders-of-magnitude increase of the charge carrier concentration while reducing the mobility value by a factor of 3.[35] These observations have been further corroborated in refs20 and 34. As proposed by Iseroff and Carter in ref 19, such an electrical resistivity decrease can be explained by the interaction between Mg and the split copper vacancy point defect $V_{Cu,split}$. Indeed, Mg tends to fill $V_{Cu,split}$, resulting in the cluster defect $I_{Mg} + 2\ V_{Cu}$.[34] Since V_{Cu} acts as a shallow acceptor, the increase copper vacancy concentration consequently explains the hole concentration improvement presented in Figure 3(a) and (b).

Upon both N and Mg doping, in Figure 3(c), we observe a decrease in the resistivity for low nitrogen incorporation (4.3 Ωcm for a N_2 flow of 2 sccm) followed by a constant increase up to 695.25 Ωcm. The first resistivity decrease is attributed to an increase of the charge carrier concentration from 8.7×10^{17} to 3.6×10^{19} cm^{-3}, which then constantly decreases to 2.8×10^{16} cm^{-3}. Complementary studies for N_2 flows lower than 4 sccm would be interesting in order to refine the trend in this region. From our analysis, we understand that while copper oxide doping using either nitrogen or magnesium enhances the material electrical properties, the co-doping strategy leads to a deterioration of the electrical conductivity due to the decrease of the charge carrier concentration. Additionally, in terms of nitrogen flow range, the conductivity degradation matches with the high nitrogen incorporation reported in the EDX measurements (see Figure 2).

Concerning the optical characterization of the 0Mg samples presented in Figure 4, we reveal a mean transparency improvement from 17.02% to 33.74% following the nitrogen

https://doi.org/10.1021/acsaelm.4c01396
ACS Appl. Electron. Mater. XXXX, XXX, XXX−XXX

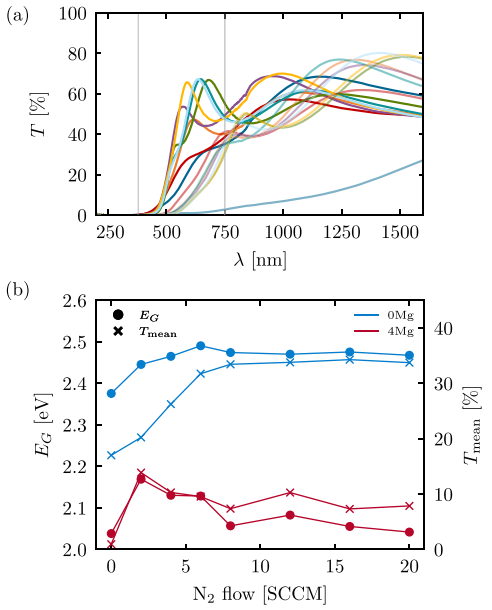

Figure 4. Optical characterization of N-doped (S2023-0, blue-highlighted "0Mg" data) and (N,Mg)-doped (S2021-4, red-highlighted "4Mg" data) thin films deposited using a N_2 flow varying between 0 and 20 sccm. Panel (a) presents the measured thin film transmittance curves. From the transmittance measurements, a Tauc plot analysis is realized and presented in Figure S3(a). Finally, from the Tauc analysis and the measured transmittance curves, the band gap and the transparency values of the deposited materials are presented in panel (b). The extracted band gap values exhibit an error margin of 0.05 eV.

flow increase. Similarly to the electrical trends reported above, this transparency enhancement is characterized by a large improvement from 0 to 6 sccm followed by a saturation for N_2 flows above 6 sccm. We also report an increase of the material band gap from 2.37 eV (0 sccm) to 2.49 eV (6 sccm) as displayed in Figure 4(b). However, as presented in Figure S3(a) in the SI, the onsets of the absorption coefficient for the 0 and 2 sccm curves are not as sharp as the ones for higher nitrogen doping values. Concerning the absorption behavior, Zhao et al. predicted an additional subband absorption peak located between 0.9 and 2 eV and attributed to the N_O point defect.[30] This prediction was experimentally observed by Malerba et al. in ref 23 but seems to be absent or not detected from the Tauc plot analysis performed in this work. On the contrary, based on the discussion supported by Figure S3 in the SI, within this energy range, we report only variations associated with interference effects. As a result, the presence of N_O point defects could not be established.

In relation to the optical properties, along with Mg doping, the material band gap decreases from 2.37 eV to 2.04 eV, an observation corroborated by Jacob et al. in ref 45. In addition, contrasting the reported electrical improvement, the Mg incorporation leads to a drastic deterioration of the thin film optical properties with an average transparency decreasing from 17.02% to below ∼1%. Then, as a result of the nitrogen incorporation in the Mg-doped layers, the mean transparency improved to values between 7.32% and 13.87% and the band gap values fluctuate around 2.1 eV (see Figure 4(b)). In addition, based on the Tauc analysis presented in Figure S3, we report a sharper onset of the absorption coefficient for N,Mg co-doped samples in opposition to the Mg-doped sample. Additionally, we present in Figure S5(b) the Haacke's figure of merit for the N-doped and (N,Mg)-doped copper oxide samples, while in Figure S5(a), we have plotted the samples' sheet resistance as a function of their average transmittance in the visible window of the spectrum (350–780 nm).

Phase and Defect Correlation through Raman Spectroscopy. Using Raman spectroscopy, possible copper oxide point defects are correlated to specific phonon vibration modes. As described by Sander et al. and Debibichi et al., the Raman activity of copper oxide material is quite interesting from the point of view of phases and point defects. Indeed, according to group theory, a pristine Cu_2O crystal only allows one phonon mode, T_{2g}, corresponding to an active Raman band located at 515 cm^{-1}.[26,46] In addition, as presented by Sander et al., a typical Raman spectrum of copper oxide Cu_2O is much richer than only the T_{2g} phonon mode. Intrinsic point

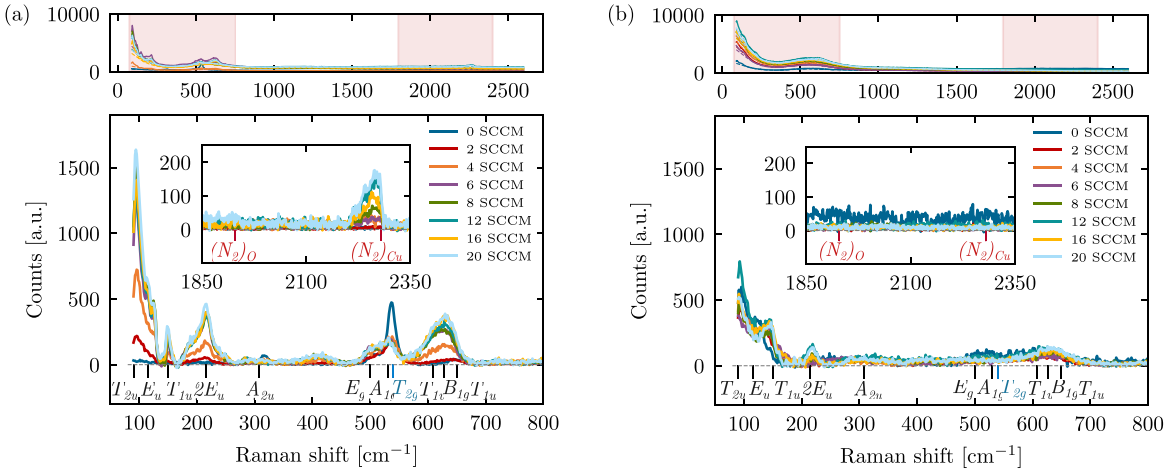

Figure 5. Raman spectra of (a) the N-doped (S2023-0) and (b) the (N,Mg)-doped (S2021-4) thin films deposited using a N_2 flow varying between 0 and 20 sccm. The top panel displays the acquired raw data, while the red highlight corresponds to zones of interest. In the bottom panels, we present the treated measurements as well as the phonon mode associated with the different Raman bands (in black). In blue, the T_{2g} mode corresponds to the only active phonon mode for a perfect copper oxide crystal.[26] In the insets, the Raman bands associated with nitrogen-related defects are shown in red. This figure is interpreted based on Table 1.

https://doi.org/10.1021/acsaelm.4c01396
ACS Appl. Electron. Mater. XXXX, XXX, XXX−XXX

defects located at different crystallographic sites possess specific local symmetries which are usually lower than the one of the perfect crystal, resulting in the activation of different Raman modes coupled to specific bands in the measured spectrum.[26,31] Among such intrinsic point defects, the most noteworthy ones are copper vacancies V_{Cu} and $V_{Cu,split}$ and oxygen vacancy V_O. Their respective Raman activities are presented in Table 1 as reported by Sander et al. in ref 26. Moreover, concerning extrinsic point defects related to Mg and N_2, one can mention the following ones in particular: Mg on $V_{Cu,split}$ as well as $(N_2)_{Cu}$ and N_O as reported in ref 24.

As pointed out by Debibichi et al., Raman spectroscopy is also an interesting analysis method to differentiate the distinct Raman response of the various copper oxide crystalline phases (CuO, Cu_4O_3, and Cu_2O).[4,46] Concerning Cu_4O_3, several Raman active modes are predicted by the group theory: A_{1g}, 541 cm^{-1}; B_{1g}, 651 cm^{-1}; and E_g, 318, 510 cm^{-1}. These theoretical predictions were also corroborated by experimental results as Wang et al. reported, upon various oxygen flow rates, Raman bands at 311, 505, and 531 cm^{-1} for the Cu_4O_3 material phase. Concerning Cu_2O, a large activity in the range between 90 and 216 cm^{-1} as well as a band located at 609 cm^{-1} were observed and can be associated with defects.[47,48]

Based on the Raman characterizations presented in Figure 5, we can suggest possible explanations concerning the microscopic origin of the charge carrier variations reported previously. Concerning the N-doped Cu_2O sample spectra shown in Figure 5(a), a distinct variation is identified between the undoped thin film (N_2 flow of 0 sccm) and the thin films synthesized with a N_2 flow parameter above 4 sccm. This behavior is further highlighted by the smooth transformation of the 0, 2, 4, and finally 6 sccm Raman spectra observed. We distinguish increased Raman activity for all bands between 90 and 250 cm^{-1} as well as for the bands located around 610 cm^{-1}. In contrast, the band at 515 cm^{-1} tends to decrease in intensity and broaden due to the splitting into two adjacent bands at 510 and 540 cm^{-1}. This observation is clearly corroborated by the results reported in refs 46−48 corresponding to a crystalline transition from Cu_4O_3 to Cu_2O.

Second, from a defect perspective, as the nitrogen flow increases, two phenomena can be observed and supported by Raman activities reported in Table 1. First, concerning intrinsic defects, the splitting of the T_{2g} mode into A_{1g} and E_g illustrates an increase of copper vacancy V_{Cu}. In addition, the increase of the Raman activity for each band below 250 cm^{-1} is attributed to an increase of $V_{Cu,split}$. Both of these observations lead to a possible explanation regarding the increase in free charge carriers previously reported. In addition to the increase of intrinsic defects, in the inset of Figure 5(a), we report a strong band activity close to 2280 cm^{-1}, which corresponds, according to Thienprasert et al., to the phonon mode of $(N_2)_{Cu}$.[24] This point defect possesses a low formation energy as well as a shallow acceptor behavior. Moreover, as the band intensity is a function of the nitrogen flow, we consequently believe that the charge carrier increase reported upon nitrogen doping is attributed to the increased concentration of $(N_2)_{Cu}$. Concerning the (N,Mg)-doped thin films presented in Figure 5(b), the Raman signatures indicate a Cu_2O material phase, as already reported in the EDX and XRD measurements. Unfortunately, the relatively poor material crystallinity does not allow us to observe any fine features that could be related to the impact of Mg doping in contrast to the results presented by Jacob et al.[45] In addition, no band activity is detected within the inset figure concerning the $(N_2)_{Cu}$ point defects.

Point Defects. First, concerning the Mg doping, from the literature, it is accepted that Mg dopant incorporates in a split copper vacancy site, forming the $I_{Mg} + 2\ V_{Cu}$ cluster defects.[19] Then regarding the nitrogen doping of free Mg samples, T-Thienprasert et al. identified N_O as a deep acceptor that cannot be responsible for the charge carrier variation reported in opposition to the shallow acceptor $(N_2)_{Cu}$ (associated with a Raman band at 2280 cm^{-1}).[24] Moreover, using Raman measurements, in this work $(N_2)_{Cu}$ point defects were clearly identified in the case of N-doped Cu_2O samples (see Figure 5(a)) with a band activity proportional to the nitrogen flow. In contrast, within the absorption spectra, no sub-band absorption corresponding to N_O was reported. Finally, concerning the (N,Mg)-doped samples, the deterioration of the crystallinity does not allow us to extract much information concerning point defects. However, in the scope of EDX measurements, we report a strong increase of the nitrogen incorporation in contrast to the Mg undoped samples. As a result, it seems that the presence of Mg facilitates the incorporation of nitrogen. A possible explanation could be that as the Mg replaces the split copper vacancy, the number of simple copper vacancies V_{Cu}, possible sites for nitrogen incorporation, also increases. The co-doping would therefore enhance the nitrogen incorporation. Indeed, that observation was realized through EDX measurements on samples synthesized with nitrogen flow values in a range that is concomitant to the amorphization reported in XRD measurements. It is thus possible that an excessive amount of nitrogen leads to the film amorphization, resulting in the subsequent degradation of the optoelectrical properties.

CONCLUSION

To conclude, this work highlights the possibility of synthesizing a Cu_2O crystalline phase starting from a CuO sputtering target. The formation of this crystalline phase can be attributed to a reduction of the oxygen inside the synthesized layers due to the lack of O flow during the RF sputtering depositions. We observe that nitrogen doping leads to a drastic reduction of the electrical resistivity from 192 to 1.15 Ωcm, concomitant with a marked improvement of the optical transparency from 17.02% to 33.74%. The former effect is mainly associated with an increase of the charge carrier concentration from 7.7×10^{16} cm^{-3} to a maximal value of 4.4×10^{20} cm^{-3} as a consequence of the increased concentration of $(N_2)_{Cu}$ shallow acceptor defects. These results are also supported by a good experimental reproducibility as presented in Figure S4 of the SI. Finally, upon Mg doping, we observe a slight improvement of the material conductivity as well as a net degradation of the thin film transparency. In addition, following the co-incorporation of Mg and N, as the nitrogen flow increases, we observe a drastic decrease of the film crystallinity. The nitrogen flow range associated with the sample amorphization corresponds to the flow range at which a high incorporation of nitrogen is reported (more than 4 times higher than in the Mg undoped thin films). This high N incorporation is also accompanied by a degradation of the electrical properties (for flow values above 2 sccm) and a slight improvement of the optical properties. As part of forthcoming research, further enhancements of the co-doping strategy, gathering the present study's insights, are to be considered to improve the material optoelectrical properties. In such subsequent work, a

https://doi.org/10.1021/acsaelm.4c01396
ACS Appl. Electron. Mater. XXXX, XXX, XXX−XXX

quantitative assessment of the relationship between the Mg,N concentrations and the amorphization degree of the thin films would deepen our understanding of related defects in Cu_2O materials.

As illustrated using Raman spectroscopy, further defect-related investigation techniques could be useful to the identification of the origin of the thin film optoelectrical behaviors. For instance, photoluminescence and advanced measurements such as positron annihilation spectroscopy (PAS) could play an interesting role in the quest for consolidating the scientific knowledge of copper oxide layers.[28] Within this context, gaining additional control over the oxygen flow would enable tuning of the layer stoichiometry. The control of the oxygen flow rate has been shown to be a crucial parameter affecting the impurity concentration as well as the film transmittance.[10] Finally, postdeposition thermal treatment in a nitrogen atmosphere is also an interesting route, specifically in the case of the (N,Mg)-doped copper oxide layers, in order to improve the sample crystallinity.[49]

■ ASSOCIATED CONTENT

Supporting Information

The Supporting Information is available free of charge at https://pubs.acs.org/doi/10.1021/acsaelm.4c01396.

1. Deposition parameters, 2. Details on characterization methods, 3. Sputtering targets' crystallinity and composition, 4. Plasma pressure optimization, 5. TOF-SIMS measurements, 6. Comment on the Tauc plot analysis, 7. Comment on S2018-0 samples, 8. Experimental reproducibility, 9. Crystallite sizes and dislocation densities, 10. Haacke's figure of merit (PDF)

■ AUTHOR INFORMATION

Corresponding Author

Thomas Ratz − *Department of Physics B5a, Q-MAT | Solid State Physics, Interfaces and Nanostructures (SPIN), University of Liege (ULiege), 4000 Liège, Belgium;* orcid.org/0000-0002-3629-1087; Email: thomas.ratz@uliege.be

Authors

Emile Fourneau − *Department of Physics B5a, Q-MAT | Experimental Physics of Nanostructured Materials (EPNM), University of Liege (ULiege), 4000 Liège, Belgium*

Naama Sliti − *Department of Physics B5a, Q-MAT | Solid State Physics, Interfaces and Nanostructures (SPIN), University of Liege (ULiege), 4000 Liège, Belgium*

Cedric Malherbe − *MolSys | Mass Spectrometry Laboratory, University of Liege (ULiege), Chemistry Institute B6c, 4000 Liège, Belgium;* orcid.org/0000-0001-5146-6706

Amaury Baret − *Department of Physics B5a, Q-MAT | Solid State Physics, Interfaces and Nanostructures (SPIN), University of Liege (ULiege), 4000 Liège, Belgium*

Benedicte Vertruyen − *CESAM | GREENMAT, Chemistry Institute B6a, University of Liège (ULiege), 4000 Liège, Belgium;* orcid.org/0000-0002-0128-7862

Alejandro V. Silhanek − *Department of Physics B5a, Q-MAT | Experimental Physics of Nanostructured Materials (EPNM), University of Liege (ULiege), 4000 Liège, Belgium;* orcid.org/0000-0001-9551-5717

Ngoc Duy Nguyen − *Department of Physics B5a, Q-MAT | Solid State Physics, Interfaces and Nanostructures (SPIN), University of Liege (ULiege), 4000 Liège, Belgium*

Complete contact information is available at: https://pubs.acs.org/10.1021/acsaelm.4c01396

Notes

The authors declare no competing financial interest.

■ ACKNOWLEDGMENTS

The authors acknowledge Dr. Guy Brammertz from IMEC division IMOMEC for the help concerning the EDX measurements. N. D. Nguyen gratefully acknowledges the financial support from F.R.S-FNRS via projects CDR J.0157.24 and PINT-MULTI R.8012.20. The work of E. Fourneau has been financially supported by the FWO and F.R.S.-FNRS under the Excellence of Science (EOS) project O.0028.22. The authors gratefully acknowledge the insightful remarks provided by the Reviewers.

■ REFERENCES

(1) Dixon, S. C.; Scanlon, D. O.; Carmalt, C. J.; Parkin, I. P. n-Type doped transparent conducting binary oxides: an overview. *Journal of Materials Chemistry C* **2016**, *4*, 6946−6961.

(2) Zhang, K. H.; Xi, K.; Blamire, M. G.; Egdell, R. G. P-type transparent conducting oxides. *J. Phys.: Condens. Matter* **2016**, *28*, 383002.

(3) Hautier, G.; Miglio, A.; Ceder, G.; Rignanese, G.-M.; Gonze, X. Identification and design principles of low hole effective mass p-type transparent conducting oxides. *Nat. Commun.* **2013**, *4*, 2292.

(4) Meyer, B.; Polity, A.; Reppin, D.; Becker, M.; Hering, P.; Klar, P.; Sander, T.; Reindl, C.; Benz, J.; Eickhoff, M.; et al. Binary copper oxide semiconductors: From materials towards devices. *physica status solidi (b)* **2012**, *249*, 1487−1509.

(5) Lakshmanan, A.; Alex, Z. C.; Meher, S. Recent advances in cuprous oxide thin film based photovoltaics. *Materials Today Sustainability* **2022**, *20*, 100244.

(6) Rühle, S. Tabulated values of the Shockley−Queisser limit for single junction solar cells. *Sol. Energy* **2016**, *130*, 139−147.

(7) Jolk, A.; Klingshirn, C. Linear and nonlinear excitonic absorption and photoluminescence spectra in Cu_2O: line shape analysis and exciton drift. *physica status solidi (b)* **1998**, *206*, 841−850.

(8) Wang, Y.; Pierson, J. F. Binary copper oxides as photovoltaic absorbers: recent progress in materials and applications. *Journal of Physics D: Applied Physics* **2021**, *54*, 263002.

(9) Mittiga, A.; Salza, E.; Sarto, F.; Tucci, M.; Vasanthi, R. Heterojunction solar cell with 2% efficiency based on a Cu_2O substrate. *Applied physics letters* **2006**, *88*, 163502.

(10) Shibasaki, S.; Honishi, Y.; Nakagawa, N.; Yamazaki, M.; Mizuno, Y.; Nishida, Y.; Sugimoto, K.; Yamamoto, K. Highly transparent Cu_2O absorbing layer for thin film solar cells. *Appl. Phys. Lett.* **2021**, *119*, 242102.

(11) Tanaka, H.; Shimakawa, T.; Miyata, T.; Sato, H.; Minami, T. Electrical and optical properties of TCO−Cu_2O heterojunction devices. *Thin solid films* **2004**, *469*, 80−85.

(12) Minami, T.; Nishi, Y.; Miyata, T.; Nomoto, J.-i. High-efficiency oxide solar cells with ZnO/Cu_2O heterojunction fabricated on thermally oxidized Cu_2O sheets. *Applied physics express* **2011**, *4*, 062301.

(13) Nishi, Y.; Miyata, T.; Minami, T. Effect of inserting a thin buffer layer on the efficiency in n-ZnO/p-Cu_2O heterojunction solar cells. *Journal of Vacuum Science & Technology A* **2012**, *30*, 04D103.

(14) Minami, T.; Nishi, Y.; Miyata, T. High-efficiency Cu_2O-based heterojunction solar cells fabricated using a Ga_2O_3 thin film as n-type layer. *Applied Physics Express* **2013**, *6*, 044101.

(15) Minami, T.; Nishi, Y.; Miyata, T. Impact of incorporating sodium into polycrystalline p-type Cu_2O for heterojunction solar cell applications. *Appl. Phys. Lett.* **2014**, *105*, 212104.
(16) Minami, T.; Miyata, T.; Nishi, Y. Relationship between the electrical properties of the n-oxide and p-Cu_2O layers and the photovoltaic properties of Cu_2O-based heterojunction solar cells. *Sol. Energy Mater. Sol. Cells* **2016**, *147*, 85−93.
(17) Minami, T.; Nishi, Y.; Miyata, T. Efficiency enhancement using a $Zn_{1-x}Ge_xO$ thin film as an n-type window layer in Cu_2O-based heterojunction solar cells. *Applied Physics Express* **2016**, *9*, 052301.
(18) Wong, T. K.; Zhuk, S.; Masudy-Panah, S.; Dalapati, G. K. Current status and future prospects of copper oxide heterojunction solar cells. *Materials* **2016**, *9*, 271.
(19) Isseroff, L. Y.; Carter, E. A. Electronic structure of pure and doped cuprous oxide with copper vacancies: suppression of trap states. *Chem. Mater.* **2013**, *25*, 253−265.
(20) Resende, J.; Jiménez, C.; Nguyen, N. D.; Deschanvres, J.-L. Magnesium-doped cuprous oxide (Mg:Cu_2O) thin films as a transparent p-type semiconductor. *physica status solidi (a)* **2016**, *213*, 2296−2302.
(21) Nolan, M.; Elliott, S. D. The p-type conduction mechanism in Cu_2O: a first principles study. *Phys. Chem. Chem. Phys.* **2006**, *8*, 5350−5358.
(22) Li, J.; Mei, Z.; Liu, L.; Liang, H.; Azarov, A.; Kuznetsov, A.; Liu, Y.; Ji, A.; Meng, Q.; Du, X. Probing defects in nitrogen-doped Cu_2O. *Sci. Rep.* **2014**, *4*, 7240.
(23) Malerba, C.; Ricardo, C. L. A.; D'Incau, M.; Biccari, F.; Scardi, P.; Mittiga, A. Nitrogen doped Cu_2O: A possible material for intermediate band solar cells. *Sol. Energy Mater. Sol. Cells* **2012**, *105*, 192−195.
(24) T-Thienprasert, J.; Limpijumnong, S. Identification of nitrogen acceptor in Cu_2O: First-principles study. *Appl. Phys. Lett.* **2015**, *107*, 221905.
(25) Paul, G.; Nawa, Y.; Sato, H.; Sakurai, T.; Akimoto, K. Defects in Cu_2O studied by deep level transient spectroscopy. *Applied physics letters* **2006**, *88*, 141901.
(26) Sander, T.; Reindl, C.; Giar, M.; Eifert, B.; Heinemann, M.; Heiliger, C.; Klar, P. Correlation of intrinsic point defects and the Raman modes of cuprous oxide. *Phys. Rev. B* **2014**, *90*, 045203.
(27) Scanlon, D. O.; Morgan, B. J.; Watson, G. W.; Walsh, A. Acceptor levels in p-type Cu_2O: rationalizing theory and experiment. *Physical review letters* **2009**, *103*, 096405.
(28) Sekkat, A.; Liedke, M. O.; Nguyen, V. H.; Butterling, M.; Baiutti, F.; Sirvent Veru, J. d. D.; Weber, M.; Rapenne, L.; Bellet, D.; Chichignoud, G.; et al. Chemical deposition of Cu_2O films with ultra-low resistivity: correlation with the defect landscape. *Nat. Commun.* **2022**, *13*, 5322.
(29) Raebiger, H.; Lany, S.; Zunger, A. Origins of the p-type nature and cation deficiency in Cu_2O and related materials. *Phys. Rev. B* **2007**, *76*, 045209.
(30) Zhao, Z.; He, X.; Yi, J.; Ma, C.; Cao, Y.; Qiu, J. First-principles study on the doping effects of nitrogen on the electronic structure and optical properties of Cu_2O. *RSC Adv.* **2013**, *3*, 84−90.
(31) Reimann, K.; Syassen, K. Raman scattering and photo-luminescence in Cu_2O under hydrostatic pressure. *Phys. Rev. B* **1989**, *39*, 11113.
(32) Wright, A.; Nelson, J. Theory of the copper vacancy in cuprous oxide. *J. Appl. Phys.* **2002**, *92*, 5849−5851.
(33) Sekkat, A.; Nguyen, V. H.; Masse de La Huerta, C. A.; Rapenne, L.; Bellet, D.; Kaminski-Cachopo, A.; Chichignoud, G.; Muñoz-Rojas, D. Open-air printing of Cu_2O thin films with high hole mobility for semitransparent solar harvesters. *Communications Materials* **2021**, *2*, 78.
(34) Resende, J.; Chaix-Pluchery, O.; Rovezzi, M.; Malier, Y.; Renevier, H.; Nguyen, N. D.; Deschanvres, J.-L.; Jiménez, C. Resilience of cuprous oxide under oxidizing thermal treatments via magnesium doping. *J. Phys. Chem. C* **2019**, *123*, 8663−8670.
(35) Sliti, N.; Fourneau, E.; Ratz, T.; Touihri, S.; Nguyen, N. D. Mg-doped Cu_2O thin films with enhanced functional properties grown by magnetron sputtering under optimized pressure conditions. *Ceram. Int.* **2022**, *48*, 23748−23754.
(36) Resende, J.; Nguyen, V.-S.; Fleischmann, C.; Bottiglieri, L.; Brochen, S.; Vandervorst, W.; Favre, W.; Jiménez, C.; Deschanvres, J.-L.; Nguyen, N. D. Grain-boundary segregation of magnesium in doped cuprous oxide and impact on electrical transport properties. *Sci. Rep.* **2021**, *11*, 7788.
(37) Ishizuka, S.; Kato, S.; Maruyama, T.; Akimoto, K. Nitrogen doping into Cu_2O thin films deposited by reactive radio-frequency magnetron sputtering. *Jpn. J. Appl. Phys.* **2001**, *40*, 2765.
(38) Lai, G.; Wu, Y.; Lin, L.; Qu, Y.; Lai, F. Low resistivity of N-doped Cu_2O thin films deposited by rf-magnetron sputtering. *Appl. Surf. Sci.* **2013**, *285*, 755−758.
(39) Mudhaffar, A.; Sultan, B.; Shalaan, E.; Al-Jawhari, H. Switching enhancement in copper oxide thin film transistors via molybdenum trioxide buffering and nitrogen doping. *J. Electron. Mater.* **2023**, *52*, 3446−3454.
(40) Ahmadi, M.; Asemi, M.; Ghanaatshoar, M. Mg and N co-doped $CuCrO_2$: A record breaking p-type TCO. *Appl. Phys. Lett.* **2018**, *113*, 242101.
(41) Almazán, C.; Vigueras Santiago, E.; López, R.; Hernández López, S.; Castrejón Sánchez, V. H.; Esparza, A.; Gómez, C. E. Cu_4O_3 thin films deposited by non-reactive rf-magnetron sputtering from a copper oxide target. *Revista mexicana de física* **2021**, *67*, 495−499.
(42) Tadjine, R.; Houimi, A.; Alim, M. M.; Oudini, N. Oxygen flow rate effect on copper oxide thin films deposited by radio frequency magnetron sputtering. *Thin Solid Films* **2022**, *741*, 139013.
(43) Patwary, M. A. M.; Saito, K.; Guo, Q.; Tanaka, T.; Man Yu, K.; Walukiewicz, W. Nitrogen doping effect in Cu_4O_3 thin films fabricated by radio frequency magnetron sputtering. *physica status solidi (b)* **2020**, *257*, 1900363.
(44) Russ, J. C. *Fundamentals of energy dispersive X-ray analysis: Butterworths monographs in materials*; Butterworth-Heinemann, 2013.
(45) Jacob, S. S. K.; Kulandaisamy, I.; Valanarasu, S.; Arulanantham, A.; Ganesh, V.; AlFaify, S.; Kathalingam, A. Enhanced optoelectronic properties of Mg doped Cu_2O thin films prepared by nebulizer pyrolysis technique. *Journal of Materials Science: Materials in Electronics* **2019**, *30*, 10532−10542.
(46) Debbichi, L.; Marco de Lucas, M.; Pierson, J.; Kruger, P. Vibrational properties of CuO and Cu_4O_3 from first-principles calculations, and Raman and infrared spectroscopy. *J. Phys. Chem. C* **2012**, *116*, 10232−10237.
(47) Wang, Y.; Ghanbaja, J.; Soldera, F.; Migot, S.; Boulet, P.; Horwat, D.; Mücklich, F.; Pierson, J. Tuning the structure and preferred orientation in reactively sputtered copper oxide thin films. *Appl. Surf. Sci.* **2015**, *335*, 85−91.
(48) Wang, Y.; Ghanbaja, J.; Bruyère, S.; Soldera, F.; Horwat, D.; Mücklich, F.; Pierson, J. Room temperature self-assembled growth of vertically aligned columnar copper oxide nanocomposite thin films on unmatched substrates. *Sci. Rep.* **2017**, *7*, 11122.
(49) Umar, M.; Swinkels, M. Y.; De Luca, M.; Fasolato, C.; Moser, L.; Gadea, G.; Marot, L.; Glatzel, T.; Zardo, I. Morphological and stoichiometric optimization of Cu_2O thin films by deposition conditions and post-growth annealing. *Thin Solid Films* **2021**, *732*, 138763.

https://doi.org/10.1021/acsaelm.4c01396
ACS Appl. Electron. Mater. XXXX, XXX, XXX−XXX